Generation of 100-TW Half-cycle Zeptosecond X-ray Pulse in cascaded regime

Chengkai Li,[1] Yunliang Wang,[1,*] Ze Chen,[1] Youyou Kang,[1]
Meiqi Sun,[1] Lipan Qin,[1] Bengt Eliasson,[2] and Xueqing Yan[3,4,5,†]

[1]*Department of Physics, School of Mathematics and Physics, University of Science and Technology Beijing, Beijing 100083, China*
[2]*SUPA, Physics Department, John Anderson Building, University of Strathclyde, Glasgow G4 0NG, Scotland, UK*
[3]*State Key Laboratory of Nuclear Physics and Technology, and Key Laboratory of HEDP of the Ministry of Education, CAPT, Peking University, Beijing 100871, China*
[4]*Beijing Laser Acceleration Innovation Center, Beijing 100871, China*
[5]*Collaborative Innovation Center of Extreme Optics, Shanxi University, Shanxi 030006, China*

(Dated: 17 September 2024; Revised 15 January 2025)

The requirement for ever shorter laser pulses is endless in ultrafast science. Here, we propose a unique mechanism to produce an ultrashort zeptosecond pulse (ZP) to break the attosecond pulse (AP) barrier, where a cascaded coherent synchrotron emission (CSE) regime of high-order harmonics generation is used for the emission of a giant half-cycle ZP. As an ultra-intense laser pulse interacts with the double foil target, a relativistic electron sheet is formed by the first foil electrons and accelerated in the transmitted direction, by which a half-cycle AP is emitted. The generated half-cycle AP continues to interact with the second foil target, where another relativistic electron sheet is formed by the second foil electrons and a giant half-cycle ZP is emitted. A theoretical model is proposed for the nanobunching mechanism of the relativistic electron sheet both in the reflected direction and in the transmitted direction, and is supported by numerical simulation results. The intensity of the ZP can reach $\sim 2.6 \times 10^{21}\,\mathrm{W/cm^2}$, with duration of 380 zs, which has a power reaching the 100-TW level. This ultraintense ZP will open the door for nuclear excitation, intra-nuclear dynamics, or vacuum physics studies in zeptosecond time scale.

I. INTRODUCTION

Benefiting from the development of chirped pulse amplification, the intensities of laser pulse can already reach relativistic intensity in excess of $10^{18}\,\mathrm{W/cm^2}$, and the peak power reaches petawatt scale at present, which has led us into the regime of relativistic nonlinear optics [1]. In the future, the high power laser will enter the exawatt or even zettawatt scale, and the intensity will be in excess of $10^{26}\,\mathrm{W/cm^2}$, which has important applications in fundemental physics [2]. The development history of ultrashort laser pulse indicates that there is an almost linear relationship between the duration and the intensity over more than 18 orders of magnitude. Accordingly, zeptosecond pulse (ZP) or yoctosecond pulse can be expected to be generated by the ultrarelativistic laser pulse interaction with ultradense plasma [3].

The development of attosecond pulse (AP) techniques have made it possible to produce picture recordings of electron dynamics outside the nucleus [4–8]. To probe the interior of the nucleus, however, it requires ZP to track the intra-nuclear dynamics and to gain access into the inner working of the nucleus on a nuclear time scale[9], such as nuclear transition, resonance internal conversion, photonuclear reaction, and nuclear optical decay [10, 11]. In addition, in the vacuum physics of quantum electrodynamics (QED) the temporal scale is the Compton time $\hbar/m_e c^2$ (on the order of zeptoseconds) with $\hbar$ being the Plank constant devided by 2π, and m_e the electron mass, and c the speed of light in vacuum. The later implies that it is also essential to have zeptosecond temporal resolution to resolve dynamical processes of electron-positron pair production and annihilation in the vacuum breakdown [12]. The gamma ray ZP can be characterized by streak cameras via pair production and quantum radiative reactions [13]. Recently, the time scale of the birth of a photoelectron wave from a molecular orbital has been demonstrated to be 247 zeptoseconds by using an electron interferometric technique [14].

As the ZP has important applications both in fundamental and applied microcosmic physics, many efforts have been made to produce ZP [15–19]. Among of them, the high-order harmonic generation (HHG) has been proven to be an effective way to produce AP or ZP with ultra-high amplitude and ultra-short duration after the coherence harmonics was recompressed [20, 21]. Shorter pulses synthesised from HHG need to acquire a broader spectrum. A way to produce higher cut-off frequency of HHG is by letting an X-ray laser pulse [22–24] or UVU laser pulse [25] interact with a muonic hydrogen atom. In fact, the interaction of X-ray laser pulses with liquid or solid plasma density, which can still be regarded as underdense plasmas in the case of X-ray driven laser pulse, can extend laser wakefield acceleration mechanism to higher acceleration gradients of TeV/cm that is about

*Electronic address: ylwang@ustb.edu.cn
†Electronic address: x.yan@pku.edu.cn

3 orders of magnitude stronger than that of the conventional plasma-based wakefield accelerations with optical lasers and gaseous materials [26, 27]. A single cycle X-ray pulse interaction with nanotube can generate relativistic electron bunches that is a powerful approach for producing photon emission in a much higher energy range [28]. In addition, the X-ray laser pulse driven wakefield acceleration can produce ultrahigh brightness attosecond electron beams[29].

Moreover, the pulse duration-intensity conjecture shows that the pulse duration will become shorter as the laser intensity grows higher[3]. In the relativistic or ultrarelativistic regime of HHG, the higher laser intensities produce much broader harmonic spectra, and the width of ZP produced by the coherent superposition of harmonics become shorter. The laser interaction with muonic hydrogen atom is an efficient way to produce HHG with high cut-off frequency[22–24]. The interaction of ultraintense laser pulse with plasma does not need to consider the limitation of laser intensity to avoid complete ionization, where the ZP can be produced by the relativistic Doppler effect in relativistic oscillating mirror (ROM) regime[30]. In the ultrarelativistic flying mirror regime, a ZP or yoctosecond pulses could be generated by X-ray laser pulses backscattered from the extremely high density mirror [3]. The relativistic flying mirror with electron density spike can emit coherent X-ray radiation in density cusps by singularity emitting radiation, of which the duration can be sub-fs [31].

As discussed above, the driven X-ray laser pulse can improve the cut-off frequency and the interaction of the ultra-intense laser pulse with plasma can produce a broader harmonic spectrum. We propose a unique mechanism that combines both of the above advantages, where a giant half-cycle ZP can be emitted by a laser pulse with normal incidence on a double-foil target. The first and second foil targets are both opaque targets. When the ultra-intense laser pulse interacts with first foil targets, an extremely dense nanometer-scale electron sheet is generated, which emits an isolated half-cycle X-ray AP in the transmitted direction in the coherent synchrotron emission (CSE) regime. When the forward AP interacts with the second foil target, a relativistic electron sheet is formed and is accelerated to ultrarelativistic speed in the reflected direction and emits a ZP. We call it the cascaded CSE (CCSE) regime for the generation of the half-cycle ZP. An advantage of the CSE regime is that its spectrum typically has a slower decay scaling $I(\omega) \propto \omega^{-4/3}$ or $I(\omega) \propto \omega^{-6/5}$ in frequency compared to the ROM regimes [32–42].

In the CCSE regime, a multi-cycle laser pulse interacting with solid target generally generates a train of AP and consequently a train of ZP. However for many application of pump-probe techniques a single AP or ZP is preferred in deed. One way to produce an intense isolated ZP is to use a one-cycle laser pulse interacting with foil. Recently, a useful compression scheme has a possibility to generate a laser pulses with focused intensities of $10^{24}\,\mathrm{W/cm^2}$ and duration of 2 fs [17].

II. EMISSION MECHANISM OF HALF-CYCLE ZP IN CCSE REGIME

A. The physical mechanism of ZP generation

Here, we describe the generation of a giant half-cycle ZP in the CCSE regime by a laser pulse with normal incidence on a double-foil target. The physical process can be divided into two stages as illustrated in Fig. 1(a). In the first stage, when the single-period ultraintense laser pulse is incident on the first foil target as illustrated in upper half of Fig. 1(a), the electrons are compressed by the laser ponderomotive force to form an electron sheet (ES) as shown in Fig. 1(d), which moves towards the bulk plasma under the ponderomotive force of the laser pulse. As a result, a transient longitudinal electrostatic field is created due to the charge separation. When the Lorentz force decreases, the Coulomb force due to the charge separation will pull the ES backwards. As the ES is accelerated in the reflected direction, it is divided into a left and right layer. The latter reverses its direction and is accelerated to ultrarelativistic velocity, and forms a relativistic electron sheet in the transmission direction, as shown in Fig. 1(d). The transmitted relativistic electron sheet (TRES) is responsible for the emission of an X-ray half-cycle AP in the CSE regime as shown in Fig. 1(e). The X-ray AP is a half-cycle pulse and has a full width at half maximum (FWHM) in time of about 10 as as shown by the close-up in the inset in Fig. 1(b).

In the second stage of the physical process, the forward X-ray AP generated by the first foil target continues to interact with the second foil target as illustrated in the lower half of Fig. 1(a). As the first foil target is opaque, the laser pulse was completely reflected by the first foil target. Only the forward AP interacts with the second foil target, which is also an opaque target. Because the generated AP is a half-cycle pulse, there is only one oscillation for the electron nanobunch around the ion background when the AP interacts with the second foil. The electron nanobunch is pushed into the bulk plasma as the Lorentz force increases, and is pulled backward when the Coulomb force increases and the the Lorentz force decreases. A relativistic electron sheet (RES) is formed from the second foil target when the electrons are accelerated in the gap of the double foil target as shown in Fig. 1(d). Then a ZP is emitted by the RES as shown in Fig. 1(e). The HHG in the CCSE regime has higher high-frequency components. We apply a spectral filter to select harmonics above 450 to obtrain the ZP. There are several alternative filters, such as polyimide-aluminum filter, carbon nanotube filters. Polyimide-aluminum filter is composed of 5200 Å of polyimide vacuum coated with 800 Å of aluminum. Carbon nanotube filters is composed of carbon nanotube foils with an atomic layer deposition film such as aluminum. By changing the density of car-

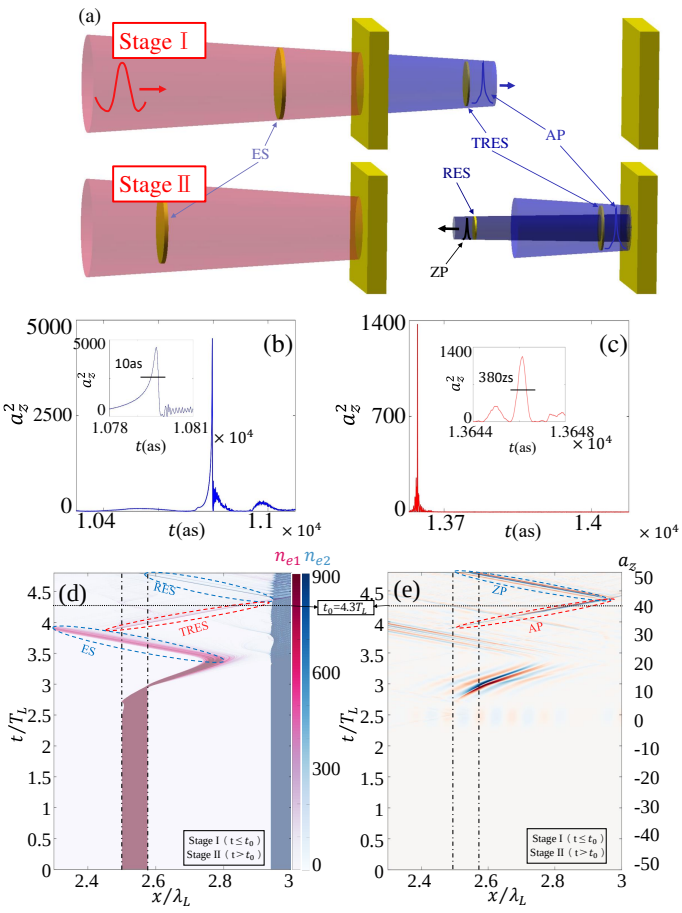

FIG. 1: (a) Schematic diagram of the two stages of ZP generation in the CCSE regime by the interaction of a laser pulse with a double foil target. (b) The intensity profile of the AP. The inset shows that the FWHM of the AP is approximately 10 as. (c) The intensity profile of the ZP obtained by a spectral filter to select harmonic number above 450. The inset shows that the FWHM of the ZP is approximately 380 zs. (d) The spatiotemporal evolution of the normalized electron number density for both targets, The electron density of the first foil target is represented in pink, and the second foil target in blue. The blue ellipse represents RES from the second foil target, while the red ellipse represents TRES from the first foil target. (e) The spatiotemporal evolution of the normalized electric field a_z after filtering. In (d) and (e), two black dash-dotted lines represent the location of the first foil target. In (d) and (e), two stages of laser plasma interaction are separated by one black dotted line, which is at $t_0 = 4.3\,T_L$. As the electron density disturbance of the second foil target is very small, the position of the second foil target is clear at a glance.

bon nanotube foil and the thickness of alumium layer, the energy range is of $50-1800\,\mathrm{eV}$[43]. The filter was placed in front of the first foil target. After the ZP was generated from the second foil target, it can be safely transmitted to the front of the first foil target. Accordingly, the detector can be set in front of the first-foil target to detect the ZP. The generated half-cycle ZP has a squared amplitude of 1227, which is normalized by $(\omega_L m_e c/e)^2$. The corresponding intensity of ZP is $2.6\times10^{21}\,\mathrm{W/cm^2}$, and the FWHM of ZP is 380 zs as shown in Fig. 1(c). Because the X-ray AP is a half-cycle pulse, only one RES is formed when the AP interacts with the second foil target, resulting in a giant isolated half-cycle ZP as seen in Fig. 1(d) and(e). From the simulation results, we can obtain that the energy of the single isolated ZP pulse is about $\sim 44\,\mu\mathrm{J}$. The energy of the driven laser pulse is $\sim 4018\,\mathrm{J}$. Then we can obtain the conversion efficiency as 10^{-8}. In fact, the conversion efficiency of the AP generation in the Stage I is about 10^{-6}.

At first glance, the CCSE regime appears to be a simple superposition of two CSE in sequence, but this is not so. The RES responsible for the generation of the ZP is accelerated by the huge electrostatic field in the gap in the double foil target, where the first layer target makes a significant contribution to the acceleration of the RES. We will discuss in detail the physical processes of the generation of ZP in the next subsection B. The key to the success of this mechanism is to generate a half-cycle X-ray AP, which is produced by the TRES from the first foil target. Even though the giant half-cycle ZP is emitted by the RES formed from the second foil target, the first foil target plays an important role in the CCSE regime. Not only is an ultra-high amplitude half-cycle X-ray AP generated by the TRES, but the RES is also continuously accelerated by the first foil to ultrarelativistic velocity.

The simulation were carried out using the particle-in-cell (PIC) code EPOCH[44]. The wavelength of the incident laser pulse is $\lambda_L = 800\,\mathrm{nm}$ with the angular frequency being $\omega_L = 2\pi c/\lambda_L$ and the period being $T_L = \lambda_L/c = 2.67\mathrm{fs}$. The laser pulse has a normalized amplitude $a_0 = eE_L/(\omega_L m_e c) = 425$, where E_L is the electric field amplitude of the laser pulse, m_e is the electron rest mass, e is the unit charge, and c is the speed of light in vacuum. The incident laser pulse has a Gaussian temporal envelope given by $a_1 = a_0 e^{-(t-T_L)^2/\tau^2}\sin[\omega_0(t-T_L)+\phi_0]$, where $\phi_0 = 4.925\,\mathrm{rad}$ is the phase of the laser pulse. Here, $\tau = 0.5\,T_L$ and $\omega_0 = \omega_L$. The length of the one-dimensional simulation box is $5\,\lambda_L$, which is resolved by 100 000 cells per wavelength. The first foil target is located at $2.5\,\lambda_L < x < 2.575\,\lambda_L$ with density $n_{e1} = 900\,n_c$, and the target thickness d_1 is 60nm. The second foil target is located at $2.9375\,\lambda_L < x < 3.025\,\lambda_L$ with density $n_{e2} = 860\,n_c$, and the target thickness d_2 is 70nm, where $n_c = \omega_L^2\epsilon_0 m_e/e^2$ is the critical density with ϵ_0 being the electric vacuum permittivity. The driven laser pulse has a normalized amplitude $a_0 = eE_L/(\omega_L m_e c) = 425$ with corresponding intensity is about $3.86\times10^{23}\,\mathrm{W/cm^2}$. At such extreme laser intensities, the QED effects should be considered in the laser plasma interaction. Accordingly, all simulations in this work have taken into account the QED effect, such as incoherent synchrotron radiation, quantum radiation reaction, and pair production.

B. The dynamics of the double foil target

Even though the giant half-cycle ZP is emitted by the RES formed from the second foil target, the first foil target plays an important role for the CCSE regime: (a) In the first stage, the ultra-high amplitude half-cycle X-ray AP is generated by the TRES, which is formed by the first foil target. (b) The transverse perturbation on the TRES comes from the radiation by the ES that is formed by the first foil target. (c) When the RES moves backward in the gap between two foils, it is continuously accelerated to ultrarelativistic velocity as a result of the huge Coulomb field in the gap, which is mainly produced by the ions from the first target. Because the ES escaped into vacuum, only ions remain at the first foil target position. Accordingly it is necessary to discuss firstly the dynamics of the first foil target when it interacts with the laser pulse.

Figure 2(a), a partial view of Fig. 1(d), illustrates the electron density n_{e1} of the first foil target when a laser pulse polarized along the z-direction is normally incident on the target. Figure 2(a) shows a relativistic oscillation of the ES under the combined actions of the laser pulse and the Coulomb force. The pondermotive force of the laser pushes the electron layer forward, while a huge electrostatic field is generated due to charge separation thus pulling the electron layer backwards and accelerating it to form an ES. The longitudinal momentum distribution of the ES is illustrated in Fig. 2(b), (c), and (d) at different times $t_1 = 3.44\,T_L$, $t_2 = 3.59\,T_L$, and $t_3 = 3.64\,T_L$, respectively, which gives a whip-shaped distribution of the longitudinal momentum distribution in the $x - p_x$ plane. The longitudinal momentum increases continuously over time. Then the ES will emit radiations in the CSE regime as shown in Fig. 1(e). The radiation from the ES will provide transverse perturbations to the TRES [47]. From Fig. 2(e), (f), and (g), the Coulomb force F_E is greater than the Lorentz force F_B , and the combined force $F_E + F_B$ is negative, which pulls the ES toward the reflection direction and makes the ES to escape to vacuum. It should be noted that most of the electrons in the first layer of the foil target are pushed out, causing the first layer of the foil target to be positively charged. This provides power for the acceleration of the RES generated by the second layer of the foil target.

When the ES move to the left side of the first foil target, the Coulomb force f_E will change its direction and become positive. For those electrons in the right half of the ES, the laser field has little action because the laser field is almost completely reflected by the front layer electron. The Coulomb force on the TRES is greater than the Lorentz force f_B as shown in Fig. 2(k), (l), and (m). Accordingly the electrons will move to the transmission direction. As a result, the separated electrons reunite after a period of time thus forming the TRES. From Fig. 2(h), (i), and (j), we can see that the longitudinal momentum of the TRES increases with time. The TRES is accelerated in the transmission direction under the action of the Coulomb force. Then the TRES will emit an X-ray AP during the acceleration, The AP propagates in the transmission direction between the two targets until it reaches and interacts with the second foil target.

Figure 3(a) illustrates the spatiotemporal evolution of the electron density n_{e2} of the second foil target under the action of the half-cycle AP generated in the first stage. The half-cycle AP interacts with the second foil target, compressing the electrons on the surface plasma layer of the second foil target to the bulk plasma, leaving the ions to generate a space charge field. The latter pulls the electron layer out of the foil target in the reflection direction to form an RES. When the RES moves between the two foil targets, it is continuously accelerated to an ultrarelativistic velocity as a result of the huge Coulomb field in the gap as shown in Fig. 3(h), (i), and (j), which is consistent with the increasing longitudinal momentum of the RES as shown in Fig. 3(e), (f), and (g). It should be pointed out that the Coulomb force is mainly produced by the ions from the first target. Because the ES has escaped into vacuum, only ions remain at the first foil target position. At the time $t_1 = 4.50\,T_L$, the RES is formed and moves in the opposite direction and a high-order harmonics starts to be generated. The HHG ends at the time $t_3 = 4.63\,T_L$. The generated high-order harmonics and the reflected AP is shown in Fig. 3(b), (c), and (d). The high-order harmonics are filtered above $450\,\omega_L$ and then we obtain an isolated half-cycle ZP.

In the above simulations, the ions are assumed to be immobile as the duration of the interaction between one-cycle laser pulse and ultrathin foil target is very short. Here we have also performed simulation with mobile ions in order to check the rationality of this assumption with the parameters about the laser plasma interaction being the same as those in Fig 1. As the ions are taken as the mobile species, we also give the spatiotemporal evolution of the ion number density as illustrated in Fig 4(a), which shows that the ions density almost keeps unchanged and has very small disturbation. It is worth pointing out that the ions was not pushed from their equilibrium position and there is no oscillation for ions. From the comparison between Fig 1(d) and Fig 4(a), the spatiotemporal evolution of the electron number density is almost identical in two cases. The extremely dense electron sheet are also produced from the first foil target and consequently the AP is also generated by the RES in the first stage in the case of mobile ions. Naturally, the ZP was also generated in the second stage as shown in Fig 4(b). The intensity profile of the ZP obtained by a spectral filter is very similar to the case of immobile ions as shown in Fig 4(c). The FWHM of the ZP is about 500 zs (as shown in Fig 4(c)) and is slightly larger than the case (380 zs) in Fig 1(c).

Here we discuss the experimental conditions and feasibility of implementing our entirely new regime of the giant half-cycle ZP generation. As the shorter pulses synthesized from HHG need to acquire a broader spectrum, we naturally want to use X-ray laser pulse interaction with plasma to produce large broad spectrum

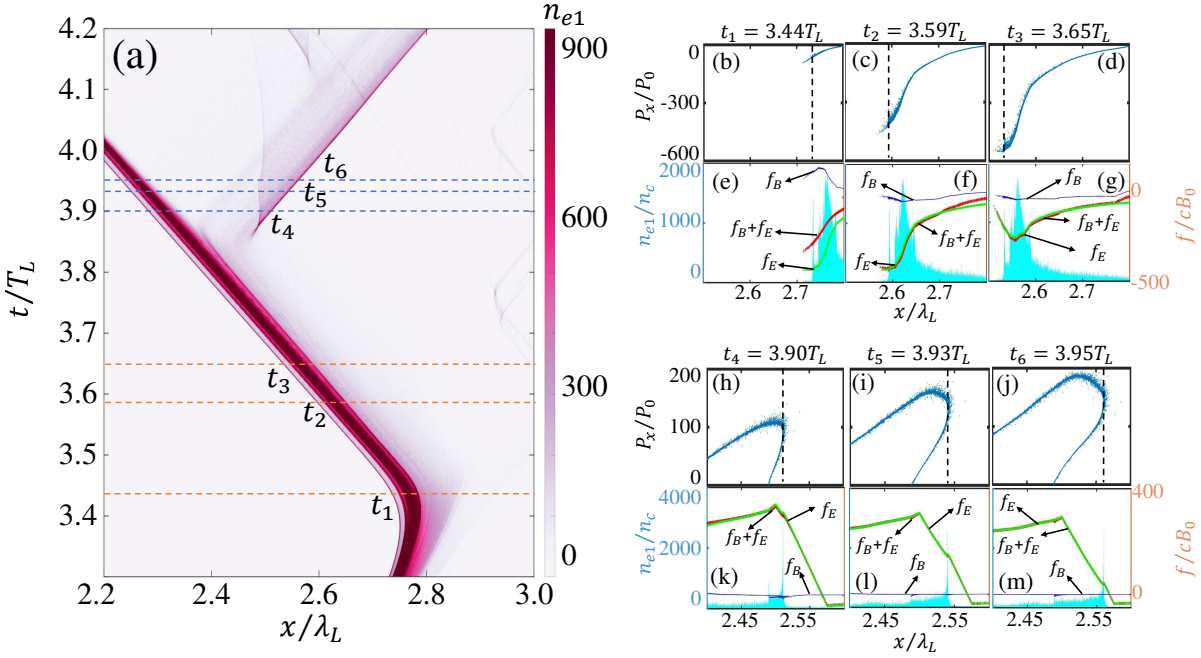

FIG. 2: (a) A close-up view of the spatiotemporal evolution of the electron density n_{e1} (normalized by n_c) of the first foil target under the action of the incident laser pulse. (b-d) The longitudinal momentum distribution of electrons in the $x-p_x$ plane at different times, $t_1 = 3.44\,T_L$, $t_2 = 3.59\,T_L$, and $t_3 = 3.64\,T_L$, respectively. The black dashed lines in (b)(d) show the profile of the electron density of the ES. (e-g) The Coulomb force f_E (green pluses), the Lorentz force f_B (blue dots), and the resultant force $f_E + f_B$ (red circles) acting on the ES at $t_1 = 3.44\,T_L$, $t_2 = 3.59\,T_L$, and $t_3 = 3.64\,T_L$, respectively. (h-j) The longitudinal momentum distribution of electrons in the $x-p_x$ plane at different times during the production process of AP, $t_4 = 3.90\,T_L$, $t_5 = 3.93\,T_L$, and $t_6 = 3.96\,T_L$, respectively. The black dashed lines in (h)(j) show the profile of the electron density of the TRES. (k-m) The Coulomb force f_E (green pluses), the Lorentz force f_B (blue dots), and the resultant force $f_E + f_B$ (red circles) acting on the TRES at $t_4 = 3.90\,T_L$, $t_5 = 3.93\,T_L$, and $t_6 = 3.96\,T_L$, respectively.

with extremely high-frequency high-order harmonics. At present, an ultarelativistic half-cycle X-ray attosecond pulse does not exist. Accordingly we propose a unique physical mechanism, which is realized by an ultra-intense one-cycle laser pulse interaction with double foil target. Thanks to the development of the optical parametric chirped-pulse amplification techniques and plasma mirrors technique, we can obtain one-cyle or few-cycle laser pulse with high contrast ratios greater than 1×10^{10} [45]. With development of the target technique, the thickness of diamond-like carbon (DLC) or gold foil can be as small as 2.9 nanometers [46].

Here, we are devoted to the generation of a single isolated ZP. Consequently, we can obtain a single ZP per driven laser pulse. Accordingly the number of ZP per second depends on the repetition rate of laser facilities. The repetition rate of relatively recent facilities at petawatt power level are able to achieve multi-Hz. To achieve higher repetition rate for petawatt power facilities, there are many new techniques proposed recently. The thulium-doped multi-pulse extraction technique is expected to increase the repetition rate to $3-5\,$kHz. Moreover, the ytterbium multi-pulse extraction technique can have repetition rate $> 50-100\,$kHz. Then we can expect that the number of ZP will be as high as 100 000 per second in the future [50].

Obviously, the key to the success of this mechanism is to generate the half-cycle AP, which was produced by the TRES from the first foil target. Even though the giant half-cycle ZP is emitted by the RES formed from the second foil target, the first foil target plays an important role for the CCSE regime. Not only is the ultra-high amplitude half-cycle X-ray AP generated by the TRES, but is the RES also continuously accelerated by the first foil to ultrarelativistic velocity. The intensity of the ZP has a power about 100 TW, which is suitable for nuclear transition, resonance internal conversion, nuclear excitation or vacuum physics studies.

III. THE THEORETICAL ANALYSIS OF ZP

A. The electrodynamics of the first ultrathin foil target

Even though the half-cycle ZP is produced by the RES formed from the second foil target, the first foil target plays an important role in the CCSE regime. On one hand, the transmitted AP is generated by the TRES formed by the first foil target. On the other hand, the half-cycle ZP is generated by the RES, which has been continuously accelerated to ultrarelativistic velocity ben-

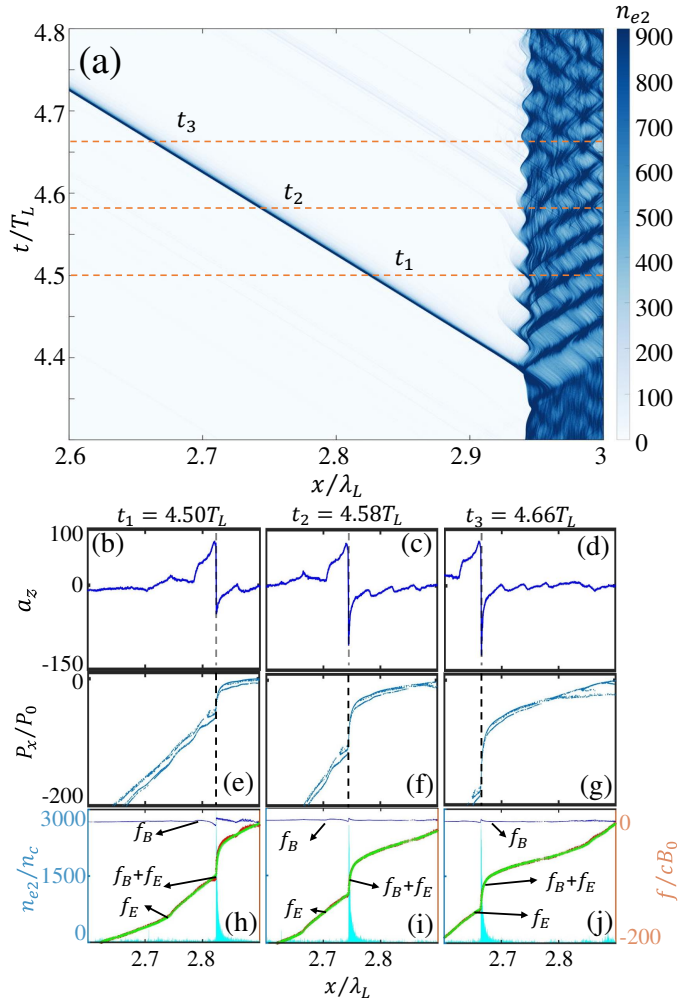

FIG. 3: (a) A close-up view of the spatiotemporal evolution of the electron density n_{e2} of the second layer foil target under the action of AP normalized by n_c. (b-d) show the profile of the ZP (blue solid line) at different times $t_1 = 4.50\,T_L$, $t_2 = 4.58\,T_L$, and $t_3 = 4.63\,T_L$, respectively. The black dashed lines in (bg) show the profile of the electron density of the RES. (e-g) show the longitudinal momentum distribution of electrons on the $x - p_x$ plane at different times during the production process of ZP, $t_1 = 4.50\,T_L$, $t_2 = 4.58\,T_L$, and $t_3 = 4.63\,T_L$, respectively. (h-j) show the Coulomb force f_E (green pluses), the Lorentz force f_B (blue dots), and the resultant force $f_E + f_B$ (red circles) acting on the RES at $t_1 = 4.50\,T_L$, $t_2 = 4.58\,T_L$, and $t_3 = 4.63\,T_L$, respectively.

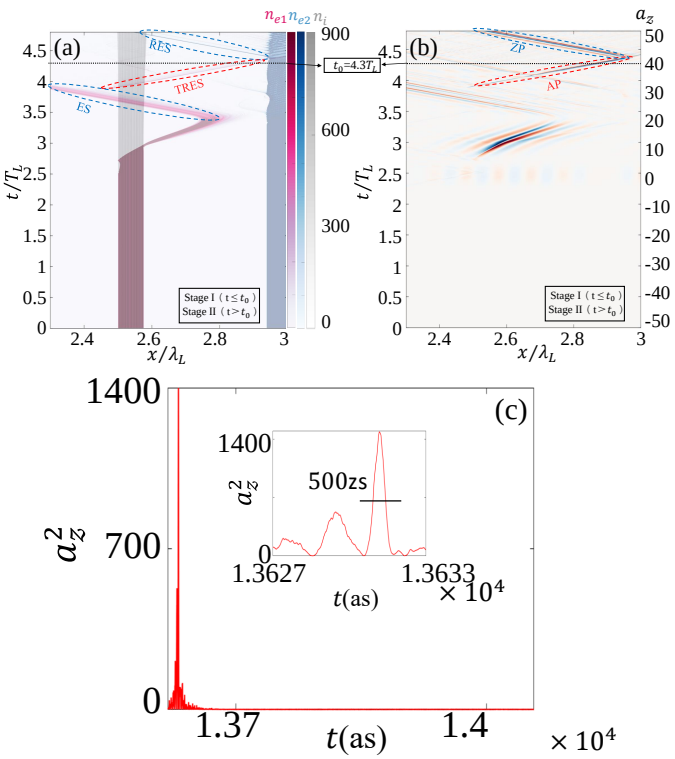

FIG. 4: (a) The spatiotemporal evolution of the normalized electron number density and ion number density. The electron density of the first foil target is represented in pink, and the second foil target is in blue. The ion density of the first foil target is represented in grey. The blue ellipse represents ES and RES from the first foil target and the second foil target, respectively. The red ellipse represents TRES from the first foil target. (b) The spatiotemporal evolution of the normalized electric field a_z after filtering. The red ellipse represents AP generated from the first foil target. The blue ellipse represents ZP from the second foil target. (c) The intensity profile of the ZP. The ZP is obtained by selecting harmonic number above 450 by spectral filter. The inset shows that the FWHM of the ZP is approximately 500 zs.

efiting from the first foil when the RES moves in the reflected direction towards the first foil target. We first analyze the relativistic dynamics of the first foil target and the formation of the TRES. The longitudinal dynamics of the first foil target are governed by the momentum equation

$$\frac{\mathrm{d}p_x}{\mathrm{d}t} = -2\pi\left(E_x - v_z B_y\right), \tag{1}$$

where the electric field E_x is normalized by $m_e\omega_L c/e$, the magnetic field B_y by $m_e\omega_L/e$, the momentum p_x by $m_e c$, and the velocity v_z by c, and time t by λ_L/c. By considering the relationship between the normalized velocity and momentum $v_z = p_z/\gamma$ and the relationship $p_z = a_z$, the last term of the right hand of Eq.(1) can be written as a_z^2/γ, where the relativistic factor is $\gamma = \sqrt{1 + p_x^2 + p_z^2} = \sqrt{1 + p_x^2 + a_z^2}$. We take time derivative of Eq.(1)

$$\frac{\mathrm{d}^2 p_x}{\mathrm{d}t^2} = -2\pi\frac{\mathrm{d}E_x}{\mathrm{d}t} - 2\pi\frac{\mathrm{d}}{\mathrm{d}t}\left(\frac{a_z^2}{\gamma}\right), \tag{2}$$

The electrostatic electric field E_x can be written as

$$E_x = 2\pi\int_{-\infty}^{x(t)} (Z_i n_{i0} - n_e(x', t))\mathrm{d}x', \tag{3}$$

where the unperturbed ion number density n_{i0} and electron number density n_e are normalized by n_c. The space

argument x and x' are normalized by λ_L. Here we assume that the unperturbed equilibrium electron number density satisfies the charge neutrality $n_{e0} = Z_i n_{i0}$. The ions remain stationary under the action of the laser pulse. Using fluid approximation, the time derivative of electrostatic electric field E_x can be simplified as [39]

$$\frac{\mathrm{d}E_x}{\mathrm{d}t} = 2\pi n_{e0} v_x, \tag{4}$$

Using Eq.(4) in Eq.(2), we obtain

$$\begin{aligned}\frac{\mathrm{d}^2 p_x}{\mathrm{d}t^2} = -4\pi^2 n_{e0}\frac{p_x}{\gamma} + 2\pi\frac{a_z^2 p_x}{\gamma^3}\frac{\mathrm{d}p_x}{\mathrm{d}t} \\ -2\pi\frac{a_z}{\gamma}\left(2-\frac{a_z^2}{\gamma^2}\right)\frac{\mathrm{d}a_z}{\mathrm{d}t}.\end{aligned} \tag{5}$$

The longitudinal relativistic oscillations of the ES formed by the first foil target can be described by Eq.(5). From Fig. 4 (a), we can see that the majority of the electrons from the first foil target are pushed from their equilibrium position towards the target by the Lorentz force of the laser pulses, which results in the formation of the ES. The Coulomb restoring force due to the displacement of the ES increases and pulls them back when the Lorentz force decreases, which results in longitudinal relativistic oscillations of the ES. The theoretical model (5) of the dynamics of the ES is numerically solved and illustrated in Fig. 4 (b). Figures 4 (a) and (b) show that the theoretical model matches well with the simulation results.

From Fig. 4 (a), when the ES reverses its direction toward the target, it is divided into a left layer and a right layer. The left layer continues to move in the reflection direction, while the right layer reverses its direction and moves in the transmission direction. The TRES is formed by the right half of the electrons in the ES, which is clearly illustrated in Fig. 4 (c) by the close-up of the spatiotemporal evolution of the electron number density n_e of the green box in Fig. 4 (a). From Fig. 2 (e), (f), and (g), we can see that the Coulomb restoring force dominates when the ES move back in the reflected direction. Especially for the electrons in the right half of the ES, the laser field has little effects on them due to that the laser field is blocked by the front layer electrons. Accordingly, the dynamics of the TRES formed by the posterior electrons in the ES is mainly dominated by electrostatic electric field force. Then we can simplify Eq.(5) for the dynamics of TRES as

$$\frac{\mathrm{d}^2 p_x}{\mathrm{d}t^2} + \frac{\Omega^2}{\gamma}p_x = 0, \tag{6}$$

where $\Omega = (4\pi^2 n_{e0})^{1/2}$. Equation (6) is a relativistic harmonic oscillation. If the longitudinal momentum of the TRES is obtained from Eq.(6), the spatial coordinates of TRES at any time is obtained as

$$x(t) = \int_0^t v_x(t')\mathrm{d}t' = \int_0^t \frac{p_x(t')}{\gamma}\mathrm{d}t'. \tag{7}$$

The evolution of the electrons in the TRES coordinates with time can be obtained from Eq.(7) as shown in Fig. 4(d), where the initial conditions are chosen as $p_z = 50$, $p_x = -300, -300.5, -301, -301.5, -302$ for the anterior layer electrons, and $p_z = 50$, $p_x = -30, -29.5, -29, -28.5, -28$ for the posterior layer of electrons. These initial conditions are selected from the simulation results in Fig. 2(b), (c), and (d). We can see that the theoretical model is consistent with the simulation results as shown in Fig. 4(c) and (d). Both the numerical simulation results as shown in Fig. 4 (c) and the theoretical mode illustrated in Fig. 4 (d) confirm that the relativistic oscillation is crucial for the formation of TRES.

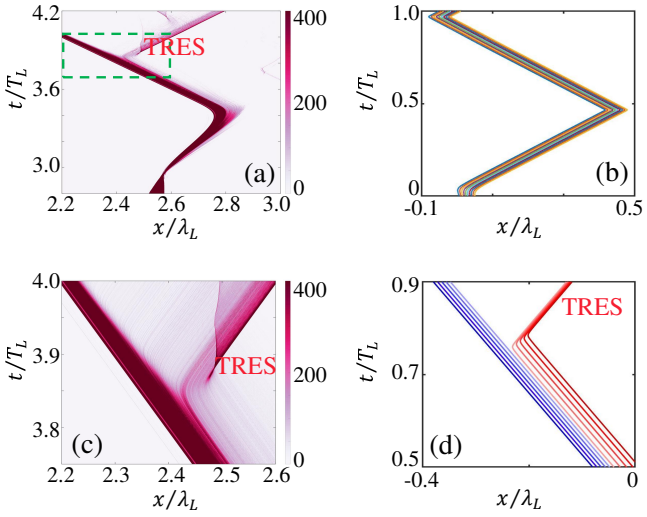

FIG. 5: (a) Simulation results of the electronic oscillation trajectory of the first layer foil target in the x-t plane. The trajectory of electrons converging into TRES on the back side of the ES. (b) An electron of the first layer foil target oscillation trajectory in the x-t plane from the analytical model. (c) Enlarged image inside the ES in (a). (d) The analytical model for the formation of TRES by electron convergence. The front layer electrons (blue) continue to move in the direction of reflection, while the back layer electrons (red) change direction opposite to that of transmission.

In Fig. 5 (d), we have chosen the initial condition $dp_x/dt \neq 0$ and taken values for different selected electrons. The electrons at different spatial positions experience different values of the electrostatic electric field. The difference in the electrostatic field between two spatial points is obtained from Eq. (3) as

$$E_{x2} - E_{x1} = 2\pi\int_{x_1}^{x_2}(n_{e0} - n_e)\mathrm{d}x'. \tag{8}$$

From Fig. 2 (e), (f), and (g), we can assume that the electron number density is similar on the right-hand side of the ES. Accordingly, we can approximately obtain the difference in the electrostatic field as $E_{x2} - E_{x1} = 2\pi(x_2 - x_1)(n_{e0} - n_e)$. Considering the difference in elec-

trostatic field, the time derivative of the longitudinal momentum dp_x/dt is different for electrons at different spatial positions. We take a time derivative of Eq.(7) and use Eq.(6) to obtain

$$\frac{\mathrm{d}x(t)}{\mathrm{d}t} = -\frac{1}{\Omega^2}\frac{\mathrm{d}^2 p_x}{\mathrm{d}t^2}. \tag{9}$$

Integrating Eq. (9) once, one obtain

$$\frac{\mathrm{d}p_x(t)}{\mathrm{d}t} = -\Omega^2\left[x(t) - x_0\right], \tag{10}$$

where x_0 is an integration constant. When $x = x_0$ at $t = 0$, we have $\mathrm{d}p_x/\mathrm{d}t = 0$. For electrons that are not at x_0 at $t = 0$, dp_x/dt is not equal to 0 and is different for electrons at different spatial positions at $t = 0$. From the simulation results shown in Fig. 4 (c), the convergence of posterior electrons are not as good as the theoretical predictions due to the difference of dp_x/dt between electrons in the TRES.

The dynamic equation (6) of relativistic harmonic oscillation can be obtained from the following Lagrangian by the variational principle

$$L = \frac{1}{2}\left(\dot{p}_x\right)^2 - \Omega^2\sqrt{1 + p_x^2 + a_z^2}, \tag{11}$$

where $\dot{p}_x$ denotes the time derivative of the longitudinal momentum. The corresponding Hamiltonian will be a constant of motion

$$H = \frac{1}{2}\left(\dot{p}_x\right)^2 + \Omega^2\sqrt{1 + p_x^2 + a_z^2} = \text{const.} \tag{12}$$

Considering the boundary condition $\dot{p}_x = 0$, $p_x = p_{x0}$, and $a_z = E_0$ at $x = x_0$, we obtain the energy integral

$$\frac{1}{2}\left(\dot{p}_x\right)^2 + \Omega^2\sqrt{1 + p_x^2 + a_z^2} = \Omega^2\sqrt{1 + p_{x0}^2 + E_0^2}. \tag{13}$$

Using Eq. (10) in Eq. (13), we obtain the energy integral in the phase space of x and p_x as

$$\frac{\Omega^2}{2}\left[x(t) - x_0\right]^2 + \sqrt{1 + p_x^2(t) + a_z^2} = \sqrt{1 + p_{x0}^2 + E_0^2}. \tag{14}$$

The energy integral equation (14) gives $x(t)$ as a function of $p_x(t)$, similar to the case of single ultrathin foil target [39]. From Eq. (14), p_x can be seen as a quadratic function of x, which is confirmed by Fig. 2(h), (i), and (j). At different times, the phase space graphs exhibit similar functional relationships between p_x and x. The latter demonstrate the rationality of the relativistic oscillation theory model for the formation of TRES.

B. The power-law exponent of ZP in CCSE regime

The ZP is emitted by the RES formed from the second foil target. The nonlinear transverse electric current of the RES formed by the second foil target determines the high-frequency spectrum of the reflected pulse in the CCSE regime[48]

$$J_z(x,t) = -2\sigma_0\delta(x - x_0(t))v_z(t), \tag{15}$$

where $x_0(t)$ represents the position of the RES at time t. Here we consider a delta function-like electric current density distribution. The reflected velocity is $v_z(t) = A_z(t)/\gamma$, where γ is the relativistic factor. A_z is the vector potential of the laser pulse and is normalized by $m_e c^2/e$. The dimensionless areal charge density is $\sigma_0 = \pi n_e d_2 \lambda$, where λ is the wavelength of the driven laser pulse, and d_2 is the second thickness of the foil target. Here, we refer to the waveform of AP as shown in Fig. 1(c) and assume $\delta_b(t)$ to represent the dimensionless electric field

$$a_z = \delta_{\tau_0}(t) = \begin{cases} a_2(1 - \frac{t^2}{\tau_0^2}), & t \in [-\tau_0, \tau_0] \\ 0, & \text{otherwise,} \end{cases} \tag{16}$$

where $\sqrt{2}\tau_0$ is FWHM of the AP, and a_2 is the laser amplitude of the AP. The relationship between the dimensionless electric field a_z and the dimensionless vector potential A_z is $a_z = -dA_z/dt$. Therefore, we can obtain the expression of A_z as

$$A_z = -a_2 t + \frac{a_2 t^3}{3\tau_0^2}. \tag{17}$$

The lowest-order approximation gives the transverse velocity as

$$v_z = -\frac{a_2 t}{\gamma} + \frac{a_2 t^3}{3\tau_0^2\gamma}. \tag{18}$$

As the RES has ultrarelativistic velocity, the absolute velocity normalized by c is close to 1. We can obtain the position of the electron beam RES by $x_0(t) = \int v_x dt$, where v_x satisfies $v_x^2 + v_z^2 = 1$, as

$$x_0(t) = t - \frac{a_2^2 t^3}{6\gamma^2} + \frac{a_2^2 t^5}{15\tau_0^2\gamma^2} - \frac{a_2^2 t^7}{126\tau_0^4\gamma^2}. \tag{19}$$

The reflected radiation can be determined by the transverse-current distribution $J_z(x,t)$ which is normalized by $en_c c$, where the profile of the transverse-current density distribution is assumed to be unchanged. The reflected field is given as[33]

$$\begin{aligned} E(t) =& -\pi\int J_z(x, t - x)dx \\ =& 2\sigma_0\pi\int v_z(t - x)\delta(x - x_0(t - x))dx. \end{aligned} \tag{20}$$

We used the highest-order term in $x_0(t)$ for Fourier transform to obtain the spectrum of the ZP as

$$I(\omega) = 8\sigma_0\pi^3\alpha_0^2(\beta\omega)^{-\frac{8}{7}}\left|Ai^{'''}(\xi)\right|^2. \tag{21}$$

where $\alpha_0 = -\frac{a_2}{3\tau_0^2\gamma}$,$\beta = \frac{1}{98\alpha_0^2}$, and $\xi = -\omega^{\frac{6}{7}}(98\omega\alpha_0^2)^{-\frac{1}{7}}$. $Ai'''(\xi) = \frac{1}{2\pi}\int \tau^3 e^{i(\xi\tau+\frac{\tau^7}{7})}d\tau$ is the third derivative of the generalized Airy function[33],where $\tau = (98\omega\alpha_0^2)^{\frac{1}{7}}t$. We note that the square of the Fourier transform of δ is 1. As Fig. 6 shows, the spectrum of the HHG-generated ZP can reach 30 000 times the fundamental frequency, where the $I(\omega) \propto \omega^{-8/7}$ scaling law for high frequencies of the spectrum is consistent with the theoretical calculations.

From Fig. 6, one can see that the harmonic spectra is slightly affected by the QED effects. The QED effects slightly enhance the intensity of high-order harmonics and is not as large as expected, which is due to the fact that there is quantum quenching of QED process in the case of short laser pulse [49]. Moreover, the double foil targets are all ultrathin targets, which is also reduces the probability of QED process. The simulation results without QED clearly shows that the QED effects slightly enhance the generation of ZP, which can be confirmed by comparing Fig. 1(c) with Fig. S1(b) in the **Supplementary materials** [51], where we can see that the duration of ZP with QED effects is slightly shorter than that without QED. Due to the presence of the QED effects, the γ-ray photons radiation is accompanied by the generation of radiation reaction effects that can compress the RES and consequently reduce the thickness of the RES. As a result, the duration of ZP with QED effects is slightly shorter than that without QED. The robustness of the CCSE regime of ZP generation is also given in the **Supplementary materials** [51].

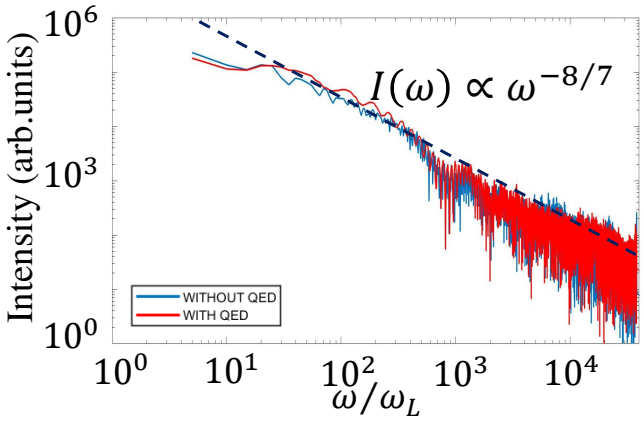

FIG. 6: The harmonic spectra of ZP. The attenuation of the spectrum follows $I(\omega) \propto \omega^{-8/7}$.

IV. CONCLUSION

We highlight an entirely new regime of the giant half-cycle ZP generation by the CCSE for the first time. As the shorter pulses synthesized from HHG need to acquire a broader spectrum, we naturally want to use X-ray laser pulse interaction with plasma to produce large broad spectrum with extremely high-frequency high-order harmonics. Accordingly we propose a unique physical mechanism including two stages, which is realized by an ultra-intense laser pulse interaction with double foil target. In stage I, a AP is firstly produced in transmission direction by the laser pulse interaction with the first foil target. The latter can produce higher cut-off frequency of high-order harmonics to synthesis giant ZP in Stage II when it interacts with the second foil target.

Obviously, the key to the success of this mechanism is to generate the half-cycle AP, which was produced by the TRES from the first foil target. Even though the giant half-cycle ZP is emitted by the RES formed from the second foil target, the first foil target plays an important role for the CCSE regime. Not only is the ultra-high amplitude half-cycle X-ray AP generated by the TRES, but also is the RES also continuously accelerated by the first foil to ultrarelativistic velocity.

We discuss in detail the dynamics of the first foil target both by the theoretical analysis and by the numerical simulation. We give the theoretical model for the AP generation in transmission direction for the first time. The electrodynamics of RES that is responsible for ZP generation is also analyzed in detail. The intensity of the ZP has a power about 100 TW, which is suitable for nuclear transition, resonance internal conversion, nuclear excitation or vacuum physics studies.

The data that support the results of this study are available on request from the authors.

Acknowledgments

We would like to thank Prof. X.L. Xu for his useful discussion. This work is supported by National Natural Science Foundation of China (NSFC) (Nos. 11974043, 11921006) and the National Grand Instrument Project (No. 2019YFF01014400) and the EUROfusion Consortium.

[1] G. A. Mourou, T. Tajima, and S. V. Bulanov, Optics in the relativistic regime, Rev. Mod. Phys. **78**, 309 (2006).
[2] G. Mourou and T. Tajima, Summary of the IZEST science and aspiration, Eur. Phys. J. Special Topics **223**, 979 (2014).
[3] G. Mourou and T. Tajima, More intense, shorter pulses, Science **331**, 41 (2011).
[4] R. Kienberger, E. Goulielmakis, M. Uiberacker, A. Baltuska, V. Yakovlev, F. Bammer, A. Scrinzi, Th. Westerwalbesloh, U. Kleineberg, U. Heinzmann, M. Drescher, F. Krausz, Atomic transient recorder, Nature, **427**, 817 (2004).

[5] M. Uiberacker, Th. Uphues, M. Schultze, A. J. Verhoef, V. Yakovlev, M. F. Kling, J. Rauschenberger, N. M. Kabachnik, H. Schrder, M. Lezius, K. L. Kompa, H.-G. Muller, M. J. J. Vrakking, S. Hendel, U. Kleineberg, U. Heinzmann, M. Drescher, F. Krausz, Attosecond real-time observation of electron tunnelling in atoms, Nature, **446**, 627 (2007).

[6] E. Goulielmakis, Z.-H. Loh, A. Wirth, R. Santra, N. Rohringer, V. S. Yakovlev, S. Zherebtsov, T. Pfeifer, A. M. Azzeer, M. F. Kling, S. R. Leone, F. Krausz, Real-time observation of valence electron motion, Nature, **466**, 739 (2010).

[7] N. Milosevic, P. B. Corkum, and T. Brabec, How to use lasers for imaging attosecond dynamics of nuclear processes, Phys. Rev. Lett. **92**, 013002 (2004).

[8] P. B. Corkum and F. Krausz, Attosecond science, Nat. phys. **3**, 381 (2007).

[9] K. Ledingham, P. McKenna, and R. Singhal, Applications for nuclear phenomena generated by ultra-intense lasers, Science **300**, 1107 (2003).

[10] R. du Rietz, D. Hinde, M. Dasgupta, R. Thomas, L. Gasques, M. Evers, N. Lobanov, and A. Wakhle, Predominant time scales in fission processes in reactions of S, Ti and Ni with W: zeptosecond versus attosecond, Phys. Rev. Lett. **106**, 052701 (2011).

[11] H. A. Weidenmüller, Nuclear Excitation by a Zeptosecond Multi-MeV Laser Pulse, Phys. Rev. Lett. **106**, 122502 (2011).

[12] T. Tajima and K. Homma, Fondamental physics explored with high intensity laser, Int. J. Mod. Phys. A, **27**, 1230027 (2012).

[13] A. Ipp, J. Evers, C. H. Keitel, and K. Z. Hatsagortsyan, Streaking at high energies with electrons and positrons, Phys. Lett. B **702**, 383 (2011).

[14] S. Grundmann, D. Trabert, K. Fehre, N. Strenger, A. Pier, L. Kaiser, M. Kircher, M. Weller, S. Eckart, and L. P. H. Schmidt, Zeptosecond birth time delay in molecular photoionization, Science **370**, 339 (2020).

[15] P. Lan, P. Lu, W. Cao, and X. Wang, Attosecond and zeptosecond x-ray pulses via nonlinear Thomson backscattering, Phys. Rev. E **72**, 066501 (2005).

[16] J. Köhler, M. Wollenhaupt, T. Bayer, C. Sarpe, and T. Baumert, Zeptosecond precision pulse shaping, Opt. Express, **19**, 11638 (2011).

[17] G. Mourou, S. Mironov, E. Khazanov, and A. Sergeev, Single cycle thin film compressor opening the door to Zeptosecond-Exawatt physics, Eur. Phys. J. Special Topics **223**, 1181 (2014).

[18] K. Krajewska, M. Twardy, and J. Z. Kamiński, Supercontinuum and ultrashort-pulse generation from nonlinear Thomson and Compton scattering, Phys. Rev. A, **89**, 032125 (2014).

[19] C. Hernández-García, J. A. Pérez-Hernández, T. Popmintchev, M. M. Murnane, H. C. Kapteyn, A. Jaron-Becker, A. Becker, and L. Plaja, Zeptosecond High Harmonic keV X-Ray Waveforms Driven by Midinfrared Laser Pulses, Phys. Rev. Lett. **111**, 033002 (2013).

[20] U. Teubner and P. Gibbon, High-order harmonics from laser-irradiated plasma surfaces, Rev. Mod. Phys. **81**, 445 (2009).

[21] F. Quéré, C. Thaury, P. Monot, S. Dobosz, P. Martin, J.-P. Geindre, and P. Audebert, Coherent wake emission of high-order harmonics from overdense plasmas, Phys. Rev. Lett. **96**, 125004 (2006).

[22] S. Chelkowski, A. D. Bandrauk, and P. B. Corkum, Muonic Molecules in Superintense Laser Fields, Phys. Rev. Lett. **93**, 083602 (2004).

[23] A. Shahbaz, C. Müller, A. Staudt, T. J. Bürvenich, and C. H. Keitel, Nuclear Signatures in High-Order Harmonic Generation from Laser-Driven Muonic Atoms, Phys. Rev. Lett. **98**, 263901 (2007).

[24] Y. Xiang, Y. Niu, Y. Qi, R. Li and S. Gong, Single zeptosecond pulse generation from muonic atoms with nonlinear chirped laser pulses, J. Mod. Opt. **57**, 385 (2010).

[25] G. K. Paramonov and P. Saalfrank, Muonic molecular ions $pp\mu$ and $pd\mu$ driven by superintense VUV laser pulses: Postexcitation muonic and nuclear oscillations and high-order harmonic generation, Phys. Rev. A **97**, 053408 (2018).

[26] X. Zhang, T. Tajima, D. Farinella, Y. Shin, G. Mourou, J. Wheeler, P. Taborek, P. Chen, F. Dollar, and B. Shen, Particle-in-cell simulation of x-ray wakefield acceleration and betatron radiation in nanotubes, Phys. Rev. Accel. Beams **19**, 101004 (2016).

[27] J. Xu, A. Buck, S.-W. Chou, K. Schmid, B. Shen, T. Tajima, M. C. Kaluza, and L. Veisz, Dynamics of electron injection in a laser-wakefield accelerator, Phys. Plasmas **24**, 083106 (2017)

[28] S. Hakimi, X. Zhang, C. Lau, P. Taborek, F. Dollar, and T. Tajima, X-ray laser wakefield acceleration in a nanotube, Int. J. Mod. Phys. A **34**, 1943011 (2019).

[29] R. Hu, Z. Gong, J. Yu, Y. Shou, M. Lv, Z. Sheng, T. Tajima, X. Yan, Ultrahigh brightness attosecond electron beams from intense X-ray laser driven plasma photocathode, in Proceedings of Workshop, "Beam Acceleration in Crystals and Nanostructures" edited by S. Chattopadhyay, G. Mourou, V. D. Shiltsev, and T. Tajima (World Scientific, 2020), p.185

[30] S. Gordienko, A. Pukhov, O. Shorokhov, and T. Baeva, Relativistic Doppler Effect: Universal Spectra and Zeptosecond Pulses, Phys. Rev. Lett. **93**, 115002 (2004).

[31] M. Kando, A. S. Pirozhkov, J. K. Koga, T. Zh. Esirkepov, and S. V. Bulanov, Prospects of relativistic flying mirrors for ultra-high-field science, Photonics **9**, 862 (2022).

[32] A. Pukhov, D. An Der Brgge, and I. Kostyukov, Relativistic laser plasmas for electron acceleration and short wavelength radiation generation, Plasma Phys. Contr. F. **52**, 124039 (2010).

[33] M. Cherednychek and A. Pukhov, Analytical approach to high harmonics spectrum in the nanobunching regime, Phys. Plasmas **23**, 103301 (2016).

[34] B. Dromey, S. Rykovanov, M. Yeung, R. Hörlein, D. Jung, D. C. Gautier, T. Dzelzainis, D. Kiefer, S. Palaniyppan, R. Shah, J. Schreiber, H. Ruhl, J. C. Fernandez, C. L. S. Lewis, M. Zepf and B. M. Hegelich, Coherent synchrotron emission from electron nanobunches formed in relativistic laser-plasma interactions, Nat. Phys. **8**, 804 (2012).

[35] B. Dromey, S. Cousens, S. Rykovanov, M. Yeung, D. Jung, D. Gautier, T. Dzelzainis, D. Kiefer, S. Palaniyppan, and R. Shah, Coherent synchrotron emission in transmission from ultrathin relativistic laser plasmas, New J. Phys. **15**, 015025 (2013).

[36] J. M. Mikhailova, M. Fedorov, N. Karpowicz, P. Gibbon, V. Platonenko, A. Zheltikov, and F. Krausz, Isolated attosecond pulses from laser-driven synchrotron radiation, Phys. Rev. Lett. **109**, 245005 (2012).

[37] M. Yeung, B. Dromey, S. Cousens, T. Dzelzainis, D.

Kiefer, J. Schreiber, J. H. Bin, W. Ma, C. Kreuzer, J. Meyer-ter-Vehn, M. J. V. Streeter, P. S. Foster, S. Rykovanov, and M. Zepf, Dependence of Laser-Driven Coherent Synchrotron Emission Efficiency on Pulse Ellipticity and Implications for Polarization Gating, Phys. Rev. Lett. **112**, 123902 (2014).

[38] S. Cousens, B. Reville, B. Dromey, and M. Zepf, Temporal structure of attosecond pulses from laser-driven coherent synchrotron emission, Phys. Rev. Lett. **116**, 083901 (2016).

[39] R. Pang, Y. Wang, X. Yan, and B. Eliasson, Ultrahigh-Amplitude Isolated Attosecond Pulses Generated in the Transmission Regime from Ultrathin Foil, Phys. Rev. Appl. **18**, 024024 (2022).

[40] S. Wei, Y. Wang, X. Yan, and B. Eliasson, Ultrahigh-amplitude isolated attosecond pulses generated by a two-color laser pulse interacting with a microstructured target, Phys. Rev. E **106**, 025203 (2022).

[41] Y. Zhang, C. L. Zhong, S. P. Zhu, X. T. He, M. Zepf, and B. Qiao, Obtaining Intense Attosecond Pulses in the Far Field from Relativistic Laser-Plasma Interactions, Phys. Rev. Applied **16**, 024042 (2021).

[42] Y. Zhang, L. Li, L.F. Gan, S.P. Zhu, X.T. He, Ph. Zeitoun, and B. Qiao, Wave-front reconstruction and analysis of far-field high-order harmonics from relativistic plasma surfaces, Phys. Rev. Applied **21**, 014058 (2024).

[43] M. Barbera, U. L. Cicero, L. Sciortino, M. Todaro, E. Puccio, F. D'Anca, N. Montinaro, S. Varisco, P. Törmä, L. Riuttanen, I. Varjos, B. Mikladal, E. Magnano, I. Pis, C. Gollwitzer, E. Handick, M. Krumrey, and C. Laubis, Carbon nanotubes thin filters for x-ray detectors in space, Proc. of SPIE **12181**, 121814H (2022).

[44] T. Arber, K. Bennett, C. Brady, A. Lawrence-Douglas, M. Ramsay, N. J. Sircombe, P. Gillies, R. Evans, H. Schmitz, and A. Bell, Contemporary particle-in-cell approach to laser-plasma modelling, Plasma Phys. Contr. F. **57**, 113001 (2015).

[45] J. M. Mikhailova, A. Buck, A. Borot, K. Schmid, C. Sears, G. D. Tsakiris, F. Krausz, and L. Veisz, Ultra-high-contrast few-cycle pulses for multipetawatt-class laser technology, Opt. lett. **36**, 3145 (2011).

[46] A. Henig, S. Steinke, M. Schnürer, T. Sokollik, R. Hörlein, D. Kiefer, D. Jung, J. Schreiber, B. M. Hegelich, X. Q. Yan, J. Meyer-ter-Vehn, T. Tajima, P. V. Nickles, W. Sandner, and D. Habs, Radiation-pressure acceleration of ion beams driven by circularly polarized laser pulses. Phys. Rev. Lett. **103**, 245003 (2009).

[47] Y. Shou, R. Hu, Z. Gong, J. Yu, J. erh Chen, G. Mourou, X. Yan, and W. Ma, Cascaded generation of isolated sub-10 attosecond half-cycle pulses, New J. Phys. **23**, 053003 (2021).

[48] V. A. Vshivkov, N. M. Naumova, F. Pegoraro, and S. Bulanov, Nonlinear electrodynamics of the interaction of ultra-intense laser pulses with a thin foil, Phys. Plasmas **5**, 2727 (1998).

[49] C. N. Harvey, A. Gonoskov, A. Ilderton, and M. Marklund, Quantum Quenching of Radiation Losses in Short Laser Pulses, Phys. Rev. Lett. **118**, 105004 (2017).

[50] C. N. Danson, C. Haefner, J. Bromage, T. Butcher, J.-C. F. Chanteloup, E. A. Chowdhury, A. Galvanauskas, L. A. Gizzi, J. Hein, D. I. Hillier, N. W. Hopps, Y. Kato, E. A. Khazanov, R. Kodama, G. Korn, R. Li, Y. Li, J. Limpert, J. Ma, C. H. Nam, D. Neely, D. Papadopoulos, R. R. Penman, L. Qian, J. J. Rocca, A. A. Shaykin, C. W. Siders, C. Spindloe, S. Szatmári, R. M. G. M. Trines, J. Zhu, P. Zhu, and J. D. Zuegel, Petawatt and exawatt class lasers worldwide, High Power Laser Sci. Eng. **7**, e54 (2019).

[51] See Supplemental Material at [URL will be inserted by publisher] for the QED effects on the generation of ZP and the robustness of the CCSE regime for the generation of ZP.